Volume 24
Number 2
14 January 2022
Pages 597–1204

PCCP

Physical Chemistry Chemical Physics

rsc.li/pccp

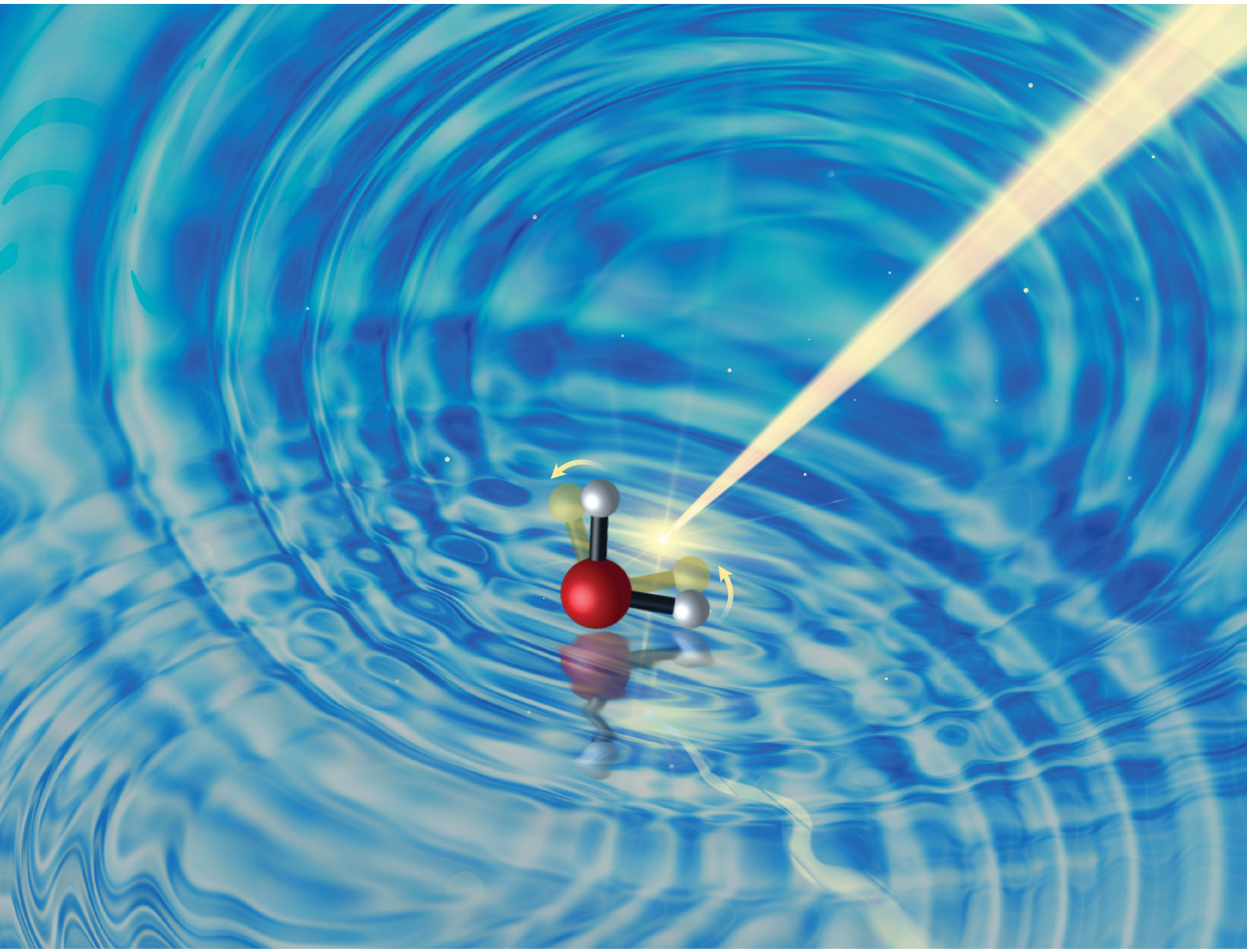

ISSN 1463-9076

ROYAL SOCIETY OF CHEMISTRY

PAPER
Fabio Novelli, Martina Havenith *et al.*
Terahertz pump–probe of liquid water at 12.3 THz

PCCP

PAPER

View Article Online
View Journal | View Issue

Cite this: *Phys. Chem. Chem. Phys.*, 2022, **24**, 653

Terahertz pump–probe of liquid water at 12.3 THz

Fabio Novelli, *[a] Claudius Hoberg,[a] Ellen M. Adams,[a] J. Michael Klopf[b] and Martina Havenith *[a]

The dynamical complexity of the hydrogen-bonded water network can be investigated with intense Terahertz (THz) spectroscopy, which can drive the liquid into the nonlinear response regime and probe anharmonicity effects. Here we report single-color and polarization-dependent pump–probe experiments at 12.3 THz on liquid water, exciting the librational mode. By comparing results obtained on a static sample and a free-flowing water jet, we are able to disentangle the distinct contributions by thermal, acoustic, and nonlinear optical effects. We show that the transient transmission by the static water layer on a time scale of hundreds of microseconds can be described by thermal (slow) and acoustic (temperature-dependent) effects. In addition, during pump probe overlap we observe an anisotropic nonlinear optical response. This nonlinear signal is more prominent in the liquid jet than in the static cell, where temperature and density perturbations are more pronounced. Our measurements confirm that the THz excitation resonates with the rotationally-damped motion of water molecules, resulting in enhanced transient anisotropy. This model can be used to explain the non-linear response of water in the frequency range between about 1 and 20 THz.

Received 14th July 2021,
Accepted 16th September 2021

DOI: 10.1039/d1cp03207k

rsc.li/pccp

Introduction

Water is one of the most studied and least understood liquids.[1] While several anomalies in the thermodynamic, macroscopic properties of liquid water are well documented,[2–4] on the microscopic scale water is characterized by a dynamical, tetrahedral network of hydrogen bonded (HB) molecules rearranging on the picosecond timescale.[5–9] Terahertz (THz) spectroscopy represents a possible experimental approach to study the water network dynamics. THz radiation is strongly absorbed[10–15] by the HB network modes[5–8] and provides a sensitive tool to study solute–solvent interactions.[16–24]

Intense THz can be used to perform nonlinear experiments and unveil the transient couplings of the different HB modes.[25–34] The first results detailing the nonlinear response of water in the THz frequency range are recent,[27,28,32,33,35] and the molecular interpretation is still a matter of ongoing discussion. Tcypkin *et al.*[32,33] performed a series of z-scan measurements at ~1 THz on liquid water and associated the third-order nonlinear signal to cascaded second-order anharmonicity of the intramolecular O–H stretching modes. Based on their model, only small variations of the nonlinear signal as a function of frequency are predicted from 0.3 to 3.5 THz (see Fig. S7 in ref. 32). Also Ghalgaoui *et al.*[35] recently measured the nonlinear response of liquid water at ~1 THz, but proposed a different explanation. They suggested that, while a water molecule experiences fluctuating electric fields of about 100 MV cm^{-1} in the bulk liquid at equilibrium, the superposition of ≥0.25 MV cm^{-1} single-cycle external fields at ~1 THz should separate and then accelerate an electron from the parent ion, leading to the ionization of water.[35]

In our previous study,[27] we focused our investigation on the frequency range of the librational mode. Experimentally, we observed a large transient anisotropy of liquid water upon librational excitation using single-color pump–probe experiments at 12.3 THz. The third order response exclusively associated to the transient birefringence, χ_ε^3, was found to exceed previously reported values in the optical range[36–53] by several orders of magnitude.[27] Accompanying simulations could rationalize these experimental results, *i.e.*, we derived an approximation of the experimental response by a simpler time evolving variable that can be calculated using molecular dynamics (MD) simulations.[27] In the classical limit, the frequency-dependent nonlinear response function of a sample, $S(\nu)$, can be written as $S(\nu) = \mathrm{FT}\left(\left\langle \frac{\mathrm{d}}{\mathrm{d}t}\cos\vartheta(t)\right\rangle\right)$, where $\vartheta(t)$ is the time-dependent angle between the direction of the applied electric field and the molecular dipole, and $\left\langle \frac{\mathrm{d}}{\mathrm{d}t}\cos\vartheta(t)\right\rangle$ indicates the average derivative of $\vartheta(t)$ in the unit volume. In other words, the response of a sample depends crucially on the orientation changes of each water dipole with respect to the external field.

[a] *Department of Physical Chemistry II, Ruhr University Bochum, 44780 Bochum, Germany. E-mail: fabio.novelli@rub.de, martina.havenith@rub.de*
[b] *Institute of Radiation Physics, Helmholtz-Zentrum Dresden-Rossendorf, Dresden, Germany*

These changes are facilitated upon excitation of the librational mode, which mainly involves a rotation of the water molecule in the surrounding hydration cage. The linear response function of liquid water was computed without external fields using MD simulations of the AMOEBA14 water model,[27] resulting in a broad spectrum extending from about 0 to 35 THz and peaking at ~17 THz (see Fig. 4 and Fig. S6 in ref. 27). We simulated the nonlinear response of water by applying an additional electric field. In this case, we found that the nonlinear signal yields a large response at the pump frequency of 12.3 THz, while the nonlinear response at 1 THz pumping is about 10*x* smaller. Thus, we proposed that the pump excitation at 12.3 THz is in resonance with the reorientation time scale of water dipoles in their hydration cages, and that applying an external field at this frequency might induce a large transient anisotropy in a homogeneous liquid phase.[27]

In our previous publication,[27] owing to a large dichroic background, we were not able to dissect the different contributions and quantify the total nonlinear response of liquid water. Therefore, in the current paper we report new measurements at 12.3 THz with long and tunable macropulses. Furthermore, we compare the results obtained in a static cell with THz-pump THz-probe measurements in a free-flowing jet. This allows us to separate thermal, acoustic, and nonlinear responses. The deduced total effective third-order response is $\chi_{\mathrm{eff}}^{3} \approx 7.2 \times 10^{-13}$ cm^2 V^{-2}, which to the best of our knowledge is the largest reported to date for liquid water in the THz range.[28,32,33,35]

Experimental

We performed pump–probe transmission experiments at 12.3 THz in pure water. We measured both a ~15 μm thick water layer in a static cell with ~0.5 mm thick diamond windows (Diamond Materials), as well as a water jet, free-flowing from a nozzle, with a ~23 μm thickness estimated from the known absorption coefficient of liquid water[10–15] at 12.3 THz, the intensity transmitted by the sample at equilibrium, and the Beer–Lambert law. The static diamond cell is magnetically attached to a copper plate that is stabilized to $20 \pm 0.05^{\circ}C$ with a chiller. The water jet uses a recirculating liquid with a total volume of about 0.5 L at room temperature (21 ± 0.1 °C) for the duration of the experiment.

The FELBE free electron laser (FEL) was operated in continuous (CW) mode at 12.3 THz, emitting a total power of approximately 10 W on the user table. The micropulses are about 3 ps long (full width at half maximum, FWHM) and the repetition rate is 13 MHz, *i.e.*, there is a ~77 ns delay between two consecutive micropulses. We used two synchronized choppers to obtain the pump and probe macropulses. The probe is chopped at 53 Hz with a duty cycle of 50%. The probe macropulses (grey in Fig. 1b) are ~9.4 ms long ("probe ON time") and separated by ~9.4 ms ("probe OFF time"). The single micropulse probe fluence is $\phi_{\mathrm{pr}} \sim 1$ μJ cm^{-2}. We chop the pump synchronously at 53 Hz with a duty cycle of 3%. The pump macropulses (green in Fig. 1b) are 283 μs long ("pump ON time") and separated by ~18.6 ms ("pump OFF time"). With the adjustable phase delay of the chopper, we set the "pump ON time" in the middle of the "probe ON time". The pump micropulse fluence is set to $\phi_{\mathrm{PU}} \sim 300$ μJ cm^{-2}, with a corresponding intensity of $I_{\mathrm{PU}} \sim \phi_{\mathrm{PU}}/(3\ \mathrm{ps}) \sim 100$ MW cm^{-2} and peak field amplitude of[54] $E_{\mathrm{PU}} = \sqrt{2 \cdot Z_0 \cdot I_{\mathrm{PU}}} \sim 0.27$ MV cm^{-1}, with $Z_0 \sim 376.7\ \Omega$ vacuum impedance.

The "ON times" of the pump (283 μs) and probe (9.4 ms) macropulses are short enough to safely avoid water boiling during a macropulse. Trivially, if boiling occurs we observe a large increase of the transmission saturating the detector, because liquid water, but not vapor, absorbs strongly at[10–15] 12.3 THz. The "OFF times" of the pump (18.6 ms) and probe (9.4 ms) macropulses are sufficiently long to ensure that the sample is equilibrated between subsequent macropulses. In fact, the thermalization time of a $l \sim 6$ μm thick water cylinder (which is about one penetration depth[10–15] at 12.3 THz) can be estimated as[55–58] $\tau_{\mathrm{th}} \sim l^2/D \sim 300$ μs, with D thermal diffusivity. Additional information about thermal effects is given in the Discussion section.

A 90-degree off-axis parabolic mirror (PM) with 2″ diameter and 75 mm effective focal length focuses both pump and probe beams into the sample. We set the linear polarization of the probe beam to an angle $\theta = 40^{\circ}$ with respect to the linear polarization of the pump beam. The pump is aligned on the vertical direction (V). The spot sizes of probe (~400 μm, $1/e^2$ diameter) and pump (~700 μm) beams were measured with a camera (Ophir Pyrocam IV). We used two additional PMs to collimate and focus the THz radiation into the detector (Judson J15D26-M204-S01M-60) and beam blockers to filter out the pump scattering. We put an analyzer–polarizer (Infraspecs P01, with polarization contrast better than 10^4:1) in front of the detector to select either the vertical (V) or horizontal (H) components of the THz probe intensity transmitted by the sample. In this way, we can measure the "vertical" ($\Delta T_{\mathrm{V}}/T_{\mathrm{V}}$) or "horizontal" pump–probe trace ($\Delta T_{\mathrm{H}}/T_{\mathrm{H}}$). With an acquisition card (National Instruments PCIe-5764), we detect the probe transmitted by the sample for 1 ms (probe acquisition time, τ, in Fig. 1b) with a resolution of 1 μs, and performed these measurements over a range of about 15 ps of pump–probe delay around the micropulse overlap time, $t \sim 0$ ps, at 0.5 ps intervals of pump–probe delay. The noise level of the transient transmission is estimated from repeated measurements to *ca.* ±0.5% (see, *e.g.*, Fig. 1c and d).

About 1% pump scattering still reaches the detector, see Fig. 2a and 3a. The scattering is a factor of five smaller than the pump–probe signals as seen in Fig. 1–3. The pump scattering was measured separately with the probe blocked, and removed as an offset from the corresponding pump–probe trace. The rise and decay times of the pump scatter, *i.e.*, the approximate time it takes for the pump macropulse to reach a plateau in the acquisition time, amounts to few microseconds.

Based on our previous results,[27] any pump frequency resonant with the relaxation time scale of the reorientation of a water molecule in its hydration cage should trigger an enhanced anisotropy in the liquid. However, there are several technical limitations. Firstly, we avoided frequency ranges with high water

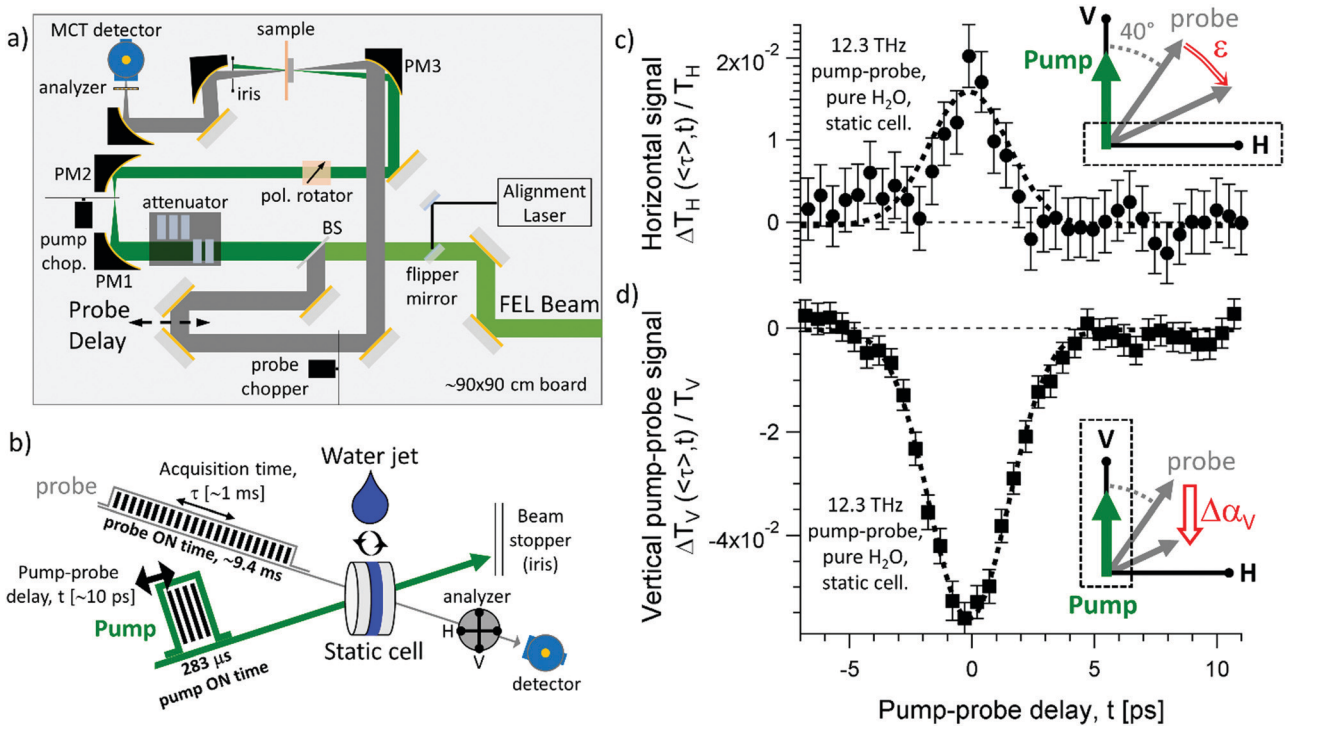

Fig. 1 Experimental setup and benchmark measurements. (a) Complete schematic diagram of the experimental setup. The FEL beam is split into the pump and probe beams and routed to the sample with a 75 mm focal parabolic mirror (PM3). The intensity and polarization of the pump beam are adjusted as needed, and a pair of parabolic mirrors with focal lengths of 75 mm (PM1) and 50 mm (PM2) reduces its size. In this way, the pump spot is safely larger than the probe spot at the sample position. The probe is delayed with a mechanical stage, and two synchronized choppers are used to control the duration of the pump and probe macropulses. (b) Zoomed in cartoon at the sample position. The pump (green) and probe (grey) macropulses are obtained with synchronized choppers. The acquisition time of the probe, τ, is about 1 ms long with 1 μs steps. The pump–probe delay, t, spans few picoseconds and refers to the pump–probe micropulse delay. We measured either water in a static cell or in a free-flowing jet, and collect the vertical (V) or horizontal (H) components of the probe radiation. (c) The horizontal pump–probe trace measured from the static cell at 12.3 THz, averaged over the pump macropulse length. It displays a positive bump at pulse overlap that is dominated by the birefringent term (ε), as established previously.[27] (d) The vertical pump–probe trace from a static water layer, averaged over the pump macropulse. The negative signal at $t \sim 0$ is mostly affected by dichroism[27] ($\Delta\alpha$). Please note that, for display purposes, we subtracted from the two traces in panels (c) and (d) the same, time-independent offset of −6.8%, which is due to the average heating of the liquid in the static cell. This effect was observed before, as detailed in the ESI of ref. 27.

vapor absorption. Secondly, we selected the central output frequency of the FEL to optimize the magnitude of the signal at the detector. Thirdly, all the optical elements used must work properly at the chosen frequency. Taking all three restrictions into consideration, we selected a single-color pump–probe frequency of 12.3 THz.

Results

In Fig. 1c and d we show the relative change of the transmitted probe intensity ($\Delta T/T$) averaged over the pump macropulse time ($\langle\tau\rangle$) and as a function of the pump–probe delay (t). As shown in Fig. 1c and d), we detect a positive (negative) pump–probe signal at pulse overlap ($t \sim 0$) when the analyzer is set to pass the horizontal (vertical) component of the probe light, $\Delta T_H(\langle\tau\rangle, t \sim 0)/T_H > 0$ ($\Delta T_V(\langle\tau\rangle, t \sim 0)/T_V < 0$). The signals are about half the magnitude of the ones we reported before, see Fig. 2 in ref. 27. We note that a quantitative comparison between the experiments reported here, performed in Dresden, with the previous ones from Nijmegen is difficult because of the different electron accelerators used. The micropulse fluence was 3.1 mJ cm^{-2} in ref. 27 and 300 μJ cm^{-2} here, while the pump macropulse duration was 8 μs in ref. 27 and 283 μs here.

In ref. 27 we observed an anisotropic signal resulting from dichroism and birefringence. In short, dichroism describes how the transient absorption coefficient ($\Delta\alpha$) varies with the polarization direction of the radiation, and the birefringence (ε) accounts for the change in polarization orientation induced by the anisotropic index of refraction. If the pump is vertically (V) polarized, the birefringent term depends on the angle (θ) between the linear polarizations of the pump and probe beams, while the dichroic term along V is unaffected. We found[27] that the magnitude of the horizontal pump–probe signal is mostly related to the birefringent term (see the inset in Fig. 1c here, or Fig. 3c in ref. 27), while the dichroism dominates the vertical pump–probe trace (see the inset in Fig. 1d here or Fig. 2a in ref. 27, which shows that $\Delta T_V/T_V$ is weakly dependent on the probe polarization angle). In order to address the origin of both the transient dichroism as well as the increase of the signal during the macropulse, we performed additional vertical pump–probe measurements ($\Delta T_V/T_V$) in a static cell (Fig. 2) and in a

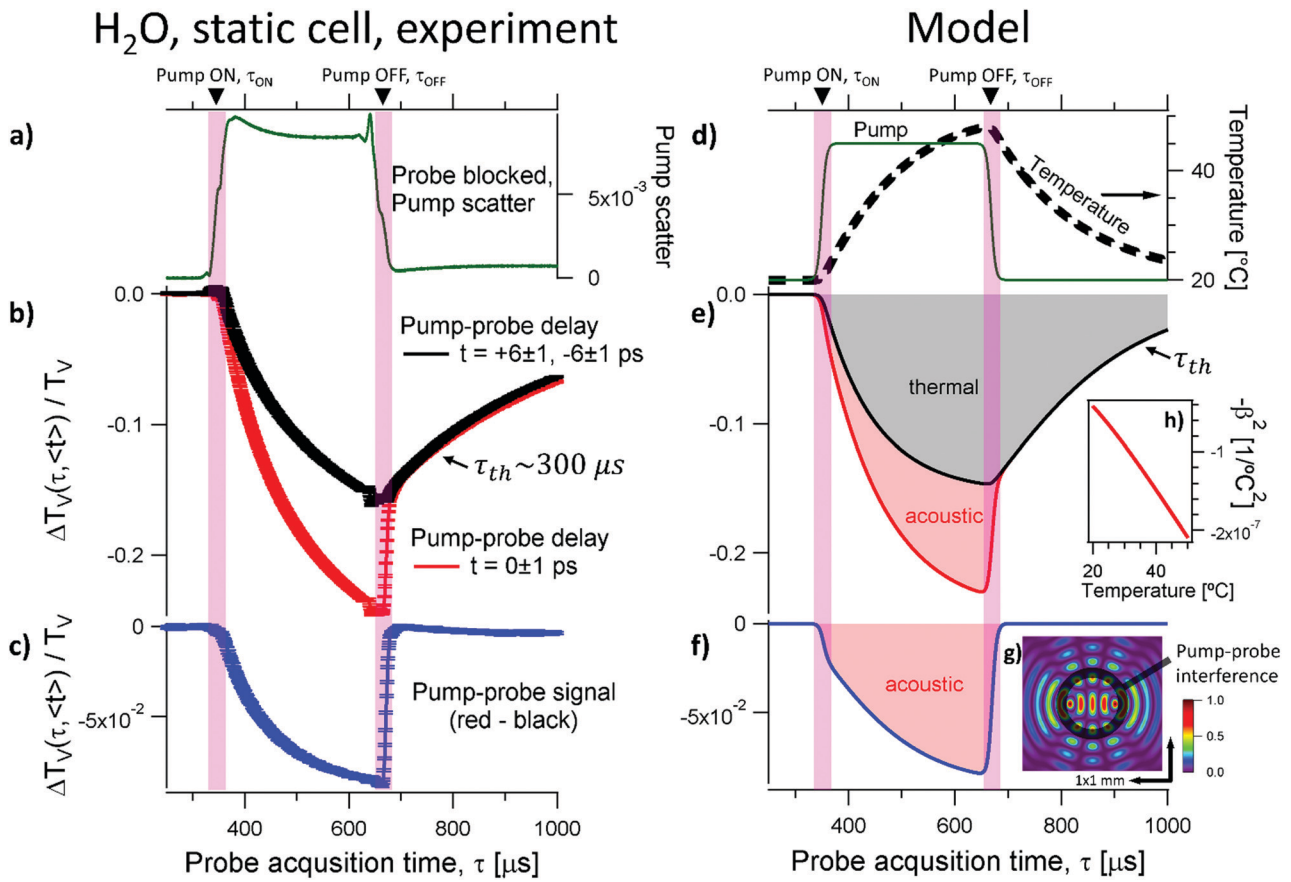

Fig. 2 Pump–probe results at 12.3 THz for water in a static cell. (a) The pump scatter shows the approximate times at which the pump is turned on (τ_{ON}) and off (τ_{OFF}). (b) Pump–probe signal as a function of the acquisition time, τ, at few significant pump–probe micropulse delays. The black line is obtained by averaging the pump–probe signal away from pulse overlap, *i.e.*, between t = +5 ps and t = +7 ps or, equivalently, t = −5 ps and t = −7 ps. The response is dominated by thermal effects with a time constant τ_{th} ∼ 300 μs. The signal at pump–probe overlap, red curve, is averaged between t = −1 ps and t = +1 ps. (c) The different response at pulse overlap is estimated by the difference between the red and black curves in panel b. (d) The temperature change of the water layer in the static cell induced by the pump pulses, as estimated from eqn (1) and (2), is shown with the thick dashed black line. The simulation uses a simple pump envelope (green). (e) The simulated variation of the transmission of the water sample induced solely by a temperature change (black curve), and including also an acoustic component (red). (f) Simulated pump–probe signal (blue), estimated as the difference of the red and black curves in panel e. (g) Color map of the calculated acoustic grating obtained at the spatial and temporal overlap of pump and probe pulses, together with surface acoustic waves propagating outwards. (h) The thermal expansivity of liquid water, $\beta(^{\circ}T)$, depends strongly on temperature.

water jet (Fig. 3). The key advantage with respect to previous experiments[27] is that the probe macropulse is longer than the pump, allowing investigation of extended dynamics.

The left column of Fig. 2 shows the results obtained from water in a static cell. Fig. 2a displays the intensity of the pump scatter (green) obtained by blocking the probe beam as a function of the acquisition time (τ). As marked by the purple bands and the black arrows, the pump macropulse is switched on approximately at τ_{ON} ∼ 370 μs, and off at τ_{OFF} ∼ 650 μs. The black curve in Fig. 2b displays the relative change of the probe transmission beyond pump–probe overlap. This is identical at positive or negative delays (see Fig. 1d at t = −6 ps and t = +6 ps). The black curve represents the responses both before (t = −6 ± 1 ps) and after (t = +6 ± 1 ps) the pump–probe overlap, averaged within ±1 ps, which are indistinguishable within the measurement error. The black curve in Fig. 2b decreases slowly after the pump is turned on ($\tau > \tau_{ON}$) and reaches a value of about $\Delta T_V/T_V \sim -15\%$ when the pump macropulse is turned off ($\tau \sim \tau_{OFF}$). After the pump is off ($\tau > \tau_{OFF}$), the signal slowly recovers with an exponential process with a time constant τ_{th} ∼ 300 μs.

The red curve in Fig. 2b displays the transient signal at pump–probe overlap, $t = 0 \pm 1$ ps. This curve decreases quickly after the pump is turned on, and reaches a value of about $\Delta T_V/T_V \sim -23\%$ just before the pump macropulse is turned off ($\tau \lesssim \tau_{OFF}$). When the pump is off ($\tau \sim \tau_{OFF}$) the signal changes abruptly, rising up to *ca.* $\Delta T_V/T_V \sim -15\%$ within few microseconds. After the pump has been turned off ($\tau > \tau_{OFF}$), the signal slowly recovers with an exponential process with a time constant τ_{th} ∼ 300 μs, *i.e.*, with the same time constant as before. The pump–probe signal can be estimated as the difference of the transient responses (red minus black trace, Fig. 2b), and is shown with the blue curve in Fig. 2c. This curve displays a slowly increasing and negative transient signal during the pump macropulse ($\tau_{ON} < \tau < \tau_{OFF}$), which keeps decreasing during the pump macropulse, in agreement with previous observations.[27]

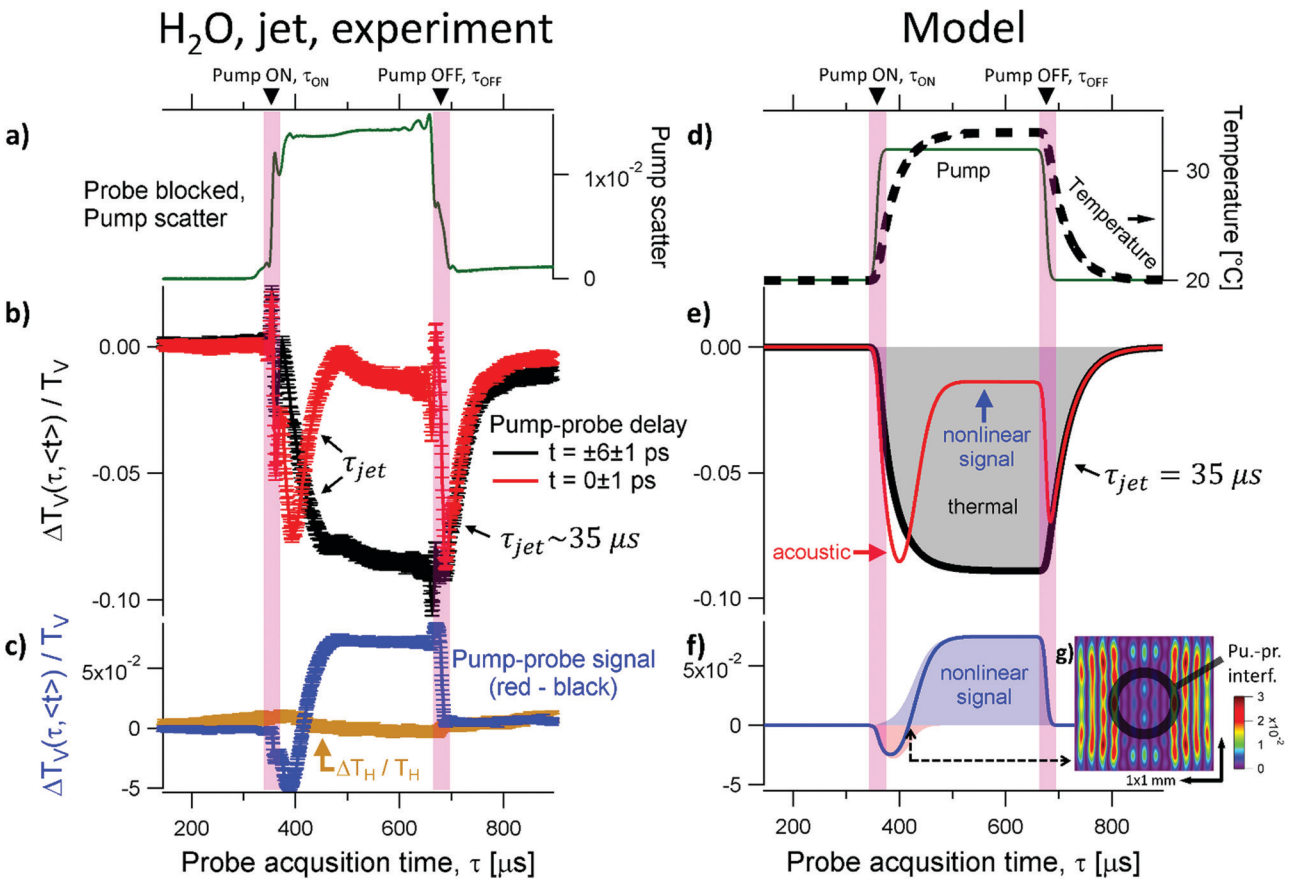

Fig. 3 Pump–probe results at 12.3 THz for water in a free-flowing jet. (a) The pump is measured by blocking the probe pulse entirely. (b) Pump–probe signal as a function of the acquisition time, τ, at few significant pump–probe micropulse delays. The black line is obtained by averaging the pump–probe signal away from pulse overlap, *i.e.*, between t = +5 ps and t = +7 ps or, equivalently, t = −5 ps and t = −7 ps. The response is dominated by the time it takes for the water to flow away, $\tau_{jet} \sim 35$ μs. The signal at pump–probe overlap, red curve, is averaged between t = −1 ps and t = +1 ps. (c) The different response at pulse overlap is estimated to the difference between the red and black curves in panel b. The orange curve is the tiny signal detected by rotating the analyzer–polarizer to transmit the horizontal component of the probe radiation. (d) The temperature change of the water layer in the jet induced by the pump pulses, and estimated from eqn (3) and (4), is shown with the thick dashed black line. The simulation uses a simple pump envelope (green). (e) The simulated variation of the transmission of the water sample induced solely by a temperature change that is determined by the jet speed (black curve), and including also acoustic (red curve, red arrow) and nonlinear optical (red curve, blue arrow) components. (f) Simulated pump–probe signal (blue), estimated as the difference of the red and black curves in panel e. (g) Estimated residue of the acoustic grating obtained by adding up patterns like the ones shown in Fig. 2g, but displaced in the vertical direction by the liquid flow, see the main text for details.

Since in a static cell the laser spot can induce a thermal gradient in the liquid, we wanted to compare these results to the ones obtained in a free flowing liquid jet. The left column of Fig. 3 shows the experimental results obtained from a free-flowing water jet. The pump–probe signal away from pulse overlap (black in Fig. 3b) quickly drops when the pump is turned on ($\tau \sim \tau_{ON}$) and, after a characteristic exponential decay with a time constant $\tau_{jet} \sim 35$ μs, will equilibrate at a negative value of $\Delta T_V/T_V = -8 \pm 1\%$ ($\tau_{ON} < \tau < \tau_{OFF}$). A weak, linear decrease of the transient transmission between about $\tau \sim 450$ μs and $\tau \sim 650$ μs might indicate an underlying, additional slow process. After the pump is off ($\tau \sim \tau_{OFF}$) the signal recovers, rising almost all the way up to $\Delta T_V/T_V \sim 0$, with a similarly fast rise time with a $\tau_{jet} \sim 35$ μs constant.

The red curve in Fig. 3b displays the transient signal at pump–probe overlap, $t = 0 \pm 1$ ps, for the water jet. This curve decreases quickly after the pump is turned on ($\tau > \tau_{ON}$), reaching a value of about $\Delta T_V/T_V \sim -7.5\%$ after approximately 35 μs from the onset of the pump macropulse ($\tau \sim \tau_{ON} + 35$ μs ~ 400 μs). The signal then reverses sign, increasing with a rise time of $\tau_{jet} \sim 35$ μs and reaching a plateau of $\Delta T_V/T_V = -1.1 \pm 0.5\%$ at $\tau \sim \tau_{ON} + 100$ μs ~ 470 μs. When the pump is turned off ($\tau \sim \tau_{OFF}$) the signal at pulse overlap (red in Fig. 3b) changes abruptly, dropping down to $\Delta T_V/T_V = -8 \pm 1\%$ within few microseconds. After the pump is off ($\tau > \tau_{OFF}$), the signal quickly recovers and approaches $\Delta T_V/T_V \sim 0$, again with a characteristic time of *ca.* $\tau_{jet} \sim 35$ μs.

The difference between the red and the black curve (see Fig. 3b) is displayed with the blue curve in Fig. 3c. This shows a fast changing and complex transient during the pump macropulse ($\tau_{ON} < \tau < \tau_{OFF}$), and a fast drop down to approximately zero, within few microseconds, when the pump is off ($\tau \sim \tau_{OFF}$). Initially, the pump–probe signal shown in blue in Fig. 3c is negative and decreasing ($\tau_{ON} < \tau < \tau_{ON} + 35$ μs) up to a

minimum turning point of $\Delta T_V/T_V \sim -5\%$ at $\tau \sim 400$ μs. After this, the signal increases and reaches a positive plateau of $\Delta T_V/T_V \sim +7\%$ (τ_{ON} + 100 μs ~ 470 μs < $\tau < \tau_{OFF}$). When the pump is turned off ($\tau \sim \tau_{OFF}$), the signal abruptly drops to zero for $\tau > \tau_{OFF}$.

For comparison, the orange curve in Fig. 3c displays the horizontal pump–probe signal ($\Delta T_H/T_H$) obtained by rotating the analyzer to transmit only the horizontal component of the probe light, while leaving all the other experimental conditions unaltered. Thus, we clearly observe an anisotropy in the polarization of the signal also in the water jet, *i.e.*, the orange and blue curves in Fig. 3c are obviously different.

Finally, we would like to point out two important details. First, the recovery times (τ_{jet} for the jet in Fig. 3, and τ_{th} for the static cell in Fig. 2) are independent on the pump–probe delay. We selected ±6 ps for display purposes only, because the pump–probe signal is centered around pulse overlap and extends only for few picoseconds around it (see Fig. 1c and d). Second, the time it takes for the signal to disappear when the pump is turned off depends also on how "sharp" the pump macropulses are in time. Given the fact that the pump macropulses are obtained with a mechanical chopper (Fig. 1a and b), the rise and decay times of the pump macropulses amount to few microseconds. See, for example, the purple bands at $\tau = \tau_{OFF}$ in Fig. 2a and 3a.

Discussion

Often, pump–probe experiments are performed with tabletop laser setups running at a repetition rate of few kilohertz. In these conditions, both thermal[55–58] ($\tau_{th} \sim 300$ μs) as well as acoustic[59,60] ($\tau_{ac} \sim 0.3$ μs as detailed in a paragraph below) effects can typically be disregarded, because they are slower than the optical nonlinear dynamics (~10 fs to ~10 ps), and faster than the delay between subsequent pulses (see, *e.g.*, the Table 4.1.1. in ref. 61). In contrast, FELs are bright but they typically operate at a repetition rate of tens of MHz, emitting macropulses lasting several microseconds. In these experimental conditions, thermal and acoustic effects can also be present,[62] together with nonlinear optical responses.[61]

In spectroscopy, thermal effects originate from the fact that the optical properties of a material can be temperature dependent.[10–12] The timescale of a thermal response is restricted by the thermal diffusivity ($D = D(^\circ T)$, which is temperature dependent) and the sample geometry. For a thin cylinder of thickness l the fastest thermalization time constant is approximately equal to[55–58] $\tau_{th} \sim l^2/D$. If we take a water cylinder with thickness given by the inverse of the absorption coefficient (α_{wat}) at 12.3 THz at the temperature $^\circ T = 20$ °C, we have $l(^\circ T = 20\ ^\circ\mathrm{C}) = \dfrac{1}{\alpha_{wat}(^\circ T = 20\ ^\circ\mathrm{C})} \sim 6$ μm, and the thermalization time is $\tau_{th}(^\circ T = 20\ ^\circ\mathrm{C}) \sim l^2(^\circ T = 20\ ^\circ\mathrm{C})/D(^\circ T = 20\ ^\circ\mathrm{C}) \sim 300$ μs. This timescale agrees very well with both the rise and decay times of the transient transmission of the static cell, away from pulse overlap (black curve in Fig. 2b). Thus, we suggest that these processes are indicative of the macroscopic thermal response.

In the following we provide semi-quantitative models in order to reproduce the magnitude and the time scales of the transient signals. The steady-state temperature increase,[63–67] $\Delta^\circ T_i$, induced by the single i-th pump micropulse in a water layer with thickness l depends on the micropulse fluence ($\phi_{PU,i}$), possible interface effects limiting the amount of absorbed radiation[67] (percentage of energy dissipated by contact with a surface, q, and/or radiation lost at interfaces due to indexes mismatch, $f(n(^\circ T))$), and the temperature-dependent specific heat of water ($C_P(^\circ T)$):

$$\Delta^\circ T_i = f(n(^\circ T)) \cdot \frac{q \cdot \phi_{PU,i}}{l \cdot C_P(^\circ T)}, \quad (1)$$

where $f(n(^\circ T)) = \dfrac{n_{dia}}{n_{air}}\left(\dfrac{2n_{air}}{n_{air}+n_{dia}}\right)^2 \dfrac{n_{wat}(^\circ T)}{n_{dia}}\left(\dfrac{2n_{dia}}{n_{air}+n_{wat}(^\circ T)}\right)^2$ are the Fresnel coefficients[68] describing the intensity transmitted at the air-diamond and diamond-water interfaces. $n_{dia} = 2.37$ is the index of refraction of diamond, $n_{air} = 1$, and n_{wat} ($^\circ T$) is the temperature-dependent index of refraction of liquid water.[10–12] We perform a simple numerical simulation in steps of 1/13 MHz ~ 77 ns, and assume that the energy of each single pump micropulse is instantaneously converted into a temperature increase of water *via* eqn (1). As we are not in steady state, this temperature gradient decays exponentially as a function of time with the thermalization constant[55–58] $\tau_{th} = l^2/D(^\circ T)$, with $l(^\circ T) = \dfrac{1}{\alpha_{wat}(^\circ T)}$ and $\alpha_{wat}(^\circ T)$ temperature-dependent absorption coefficient.[10–12] The black dashed curve in Fig. 2d shows the transient temperature of the water layer during the pump macropulse, estimated from eqn (2):

$$^\circ T(\tau) = \sum_i \Delta^\circ T_i \cdot e^{-\tau/\tau_{th}}, \quad (2)$$

that is obtained by summing up the contributions of all the pump micropulses (i). All but one of the quantities needed to calculate eqn (2) are taken from the literature ($C_P(^\circ T)$ and $D(^\circ T)$ from ref. 69, $n_{wat}(^\circ T)$ and $\alpha_{wat}(^\circ T)$ from ref. 10) or from the experimental parameters reported in the Methods section ($\phi_{PU} \sim 300$ μJ cm^{-2}). While we fixed these values, we fitted the percentage amount of heat dissipated to the diamond windows (q). The precise calculation of these thermalization processes is complex[65] because the sample is not in thermodynamic equilibrium, there are interactions between diamond and water at their interface, and because the static cell is magnetically attached to a copper plate that is, in turn, temperature-stabilized with a chiller. Choosing the fitting parameter $q = 40\%$ yields the best results. The simulated temperature change is shown as the black line in Fig. 2d, on the right scale. From this temperature profile and the Beer–Lambert law, we simulate the resulting change of the liquid transmission at 12.3 THz, see the solid black line in Fig. 2e. Thus, we are able to reproduce the size and the time variation of the transient response by liquid water for $t = \pm 6$ ps before and after the pump–probe overlap. When we compare the black curve in Fig. 2b with the model, black curve in Fig. 2e, we find good agreement for $\tau > 700$ μs. However, the experimentally

detected fast change of the transient signal at pump–probe overlap cannot be explained by thermalization.

Optoacoustic effects originate from the fact that the optical properties of a medium can change as a result of density variations,[62] which can trigger the generation of acoustic waves.[70–76] When radiation is strongly absorbed, as in the case of Terahertz spectroscopy on liquid water,[59,60] thermoacoustic effects dominate. In first approximation, the absorption triggers thermal expansion that, in turn, can induce a pressure wave with associated mass displacement and density perturbations.[59,60,63–67,71,76–83] The timescale of an acoustic phenomenon is determined by the speed of sound[84] ($v \sim 1500$ m s^{-1} for liquid water at 20 °C) and the sample geometry. The time it takes for a surface acoustic wave (moving on the surface of the liquid water sample, perpendicular to the optical table) to travel through the probe spot size ($\sim$400 μm) is $\tau_{ac} \sim \frac{400\ \mu m}{1500\ m\ s^{-1}} \sim 0.3$ μs. The amplitude of a propagating acoustic wave is proportional to the coefficient of thermal expansion,[67] $\beta = \beta(^{\circ}T)$, which is strongly dependent on temperature in liquid water (Fig. 2h). Thus, the increase of the signal at pump–probe overlap during the pump macropulse, and the abrupt drop when the pump is turned off, are both consistent with an acoustic phenomenon (see the red curve in Fig. 2b, and the blue curve in Fig. 2c, between τ_{ON} and τ_{OFF}).

When the pump and probe beams overlap in space and time, their interference can induce a grating.[85] This could account for the experimental fact that the pump–probe signal is present only at pulse overlap ($t \sim 0$ in Fig. 1–3). The spatial period (Λ) of the interference pattern depends on the laser wavelength (λ), and the angle between the propagation directions of the pump and probe beams (ψ), $\Lambda = \frac{\lambda}{2\sin\left(\frac{\psi}{2}\right)}$ (see, *e.g.*, paragraph 2.2.1 in ref. 85). In our case, considering the experimental parameters, the period of the interference pattern at pump probe pulse overlap is $\Lambda \sim 180$ μm, which can be compared with the probe spot size of $\sim$400 μm. The intensity modulation of the interference pattern, which is the relative variation between maxima and minima, can be estimated by the ratio between the electric field amplitudes[85] of probe and pump as $4\sqrt{\frac{\phi_{pr}}{\phi_{PU}}} \sim 23\%$. The transient gratings have different relaxation timescales.[78,79,85–88] An acoustic grating[67,78–82] is strongly dependent on temperature (Fig. 2h), and decays quickly, on a timescale of $\tau_{ac} \sim 0.3$ μs. A thermal grating decays on a much longer timescale,[78,79] determined by $\tau_{th} \sim 300$ μs. Considering the short laser pulses used here (FWHM $\sim$ 3 ps) and the $\sim$77 ns delay between subsequent micropulses, the contribution by the acoustic grating should be much larger than that of a thermal grating.[62] A simplistic cartoon of the acoustic grating generated at the water surface is given in Fig. 2g, which is obtained by taking two separate point sources of spherical waves[68] within the laser spot. This qualitative model includes both the interference region at the spatial and temporal overlap of pump and probe (indicated by the black circle, ''Pump–probe interference''), as well as the propagation of acoustic waves on the surface, away from the interference region.[78]

In our previous study we found[27] that all the pump–probe signals from liquid water at 12.3 THz are proportional to the pump intensity and are independent from the probe. This is consistent with any process that requires two pump photons and one probe photon, which includes the diffraction of a pump photon from a transient grating. The pump photon diffracted in the probe direction can either enhance or suppress the transmitted intensity, depending on the sign of the coupling term (see, *e.g.*, paragraph 7.4 and eqn (7.4.15) in ref. 61). The amount of scattered light depends on the diffraction efficiency (η), which is proportional to the square of the modulation of the index of refraction ($\eta \propto \Delta n^2$) induced in the sample by the intensity pattern.[78] In turn, the change in the index of refraction is proportional to the density variation ($\Delta n \propto \Delta\rho$),[59,78] and the acoustic density perturbation scales linearly with the thermal expansion coefficient ($\Delta\rho \propto \beta(^{\circ}T)$).[67,78–82] Thus, the contribution from an acoustic grating to the detected pump–probe signal from liquid water should be proportional to[67,78] $\beta^2(^{\circ}T)$. In order to obtain the red curve in Fig. 2e, we take the change in temperature as given by the black curve in Fig. 2e, and add a term $b\beta^2(^{\circ}T)$, where b is a fitting parameter. By fixing $b = -1.5 \times 10^4$, it is possible to qualitatively reproduce the experimentally observed trend and the size of the pump–probe signal from liquid water in the static cell at pump–probe overlap ($t \sim 0$). Compare the red curves in Fig. 2b and e, and the blue curves in Fig. 2c and f.

We expect a different result in case of a free-flowing water jet. In this case, the thermalization is restricted by the speed of the jet, rather than by thermal diffusion. When the water has travelled by about one full laser spot size, the temperature within the probed volume is equilibrated at an average temperature, which remains constant as long as the laser pump macropulse is on. The water flow of the jet amounts to *ca.* 2.9×10^3 mm^3 s^{-1}. The syringe tip used as nozzle has an initial radius of 0.4 mm. The tip is squeezed with pliers to the shape of a few micrometre thin slit, and was optimized with a trial-and-error approach to obtain a flat profile. Here, we give a rough over-estimate of the jet speed by assuming a perfectly round nozzle. With this approximation, the time (τ_{jet}) it takes for the jet to move one full probe spot size away (400 μm) is smaller than $400\ \mu m \Big/ \left(\frac{2.9 \times 10^3\ mm^3\ s^{-1}}{\pi(0.4\ mm)^2}\right) \sim 70$ μs. Thus, we find good agreement of the decay constant of the signal observed at $\tau > \tau_{OFF}$ (see the black curve in Fig. 3b) with the travel time of the jet, $\tau_{jet} \sim 35$ μs. We stress that the same time constant is observed when the pump macropulse is off for both the black and the red curves in Fig. 3b, and at $\tau \sim 400$ μs at pump–probe overlap (red curve in Fig. 3b). We note that changing the flow rate is expected to change τ_{jet}. However, we found that changing the speed strongly affects the shape, dimensions, and the fluctuations of the jet. As the jet is only stable enough at a flow speed close to 2.9×10^3 mm^3 s^{-1}, in the current experiments we could not reliably measure how τ_{jet} depends on the jet velocity.

We can now extend the thermal model developed above (eqn (1) and (2)). The temperature increase triggered by a single pump micropulse in the water jet is

$$\Delta^{\circ}T_i = g(n(^{\circ}T)) \cdot \frac{\phi_{\mathrm{PU},i}}{l \cdot C_{\mathrm{P}}(^{\circ}T)}, \quad (3)$$

where $g(n(^{\circ}T)) = \frac{n_{\mathrm{wat}}(^{\circ}T)}{n_{\mathrm{air}}}\left(\frac{2n_{\mathrm{air}}}{n_{\mathrm{air}} + n_{\mathrm{wat}}(^{\circ}T)}\right)^2$, because there is only an air–water interface. Please note that there is no energy dissipated by contact to a temperature-stabilized diamond surface, so the parameter q is absent in eqn (3). The temperature profile expected for the jet is akin to eqn (2),

$$^{\circ}T(\tau) = \sum_i \Delta^{\circ}T_i \cdot \mathrm{e}^{-\tau/\tau_{\mathrm{jet}}}, \quad (4)$$

with the difference that the timescale is determined by the jet speed, τ_{jet} = 35 μs. The black dashed curve in Fig. 3d is the transient temperature of the water jet during the pump macropulse, as calculated from eqn (3) and (4). The corresponding, estimated change of the liquid transmission at 12.3 THz is displayed by the solid black line in Fig. 3e. Thus, we conclude that this thermal model is able to reproduce the size and the trend of the transient transmission of the water jet away from pump–probe overlap. Compare the experiment, black curve in Fig. 3b, with the model, black curve in Fig. 3e. Please note that in this simulation there are no fitting parameters.

We expect different acoustic effects in a free-flowing jet with respect to water in a static cell. The interference of a pair of pump and probe micropulses interacting with the liquid at spatial and temporal overlap would result in patterned surface acoustic waves as shown in the color map in Fig. 2g. However, the following pulses will "write" a spatially shifted pattern, since water has travelled a distance $\frac{2.9 \times 10^3\ \mathrm{mm^3\ s^{-1}}}{\pi(0.4\ \mathrm{mm})^2} \cdot 77\ \mathrm{ns} \sim$ 0.44 μm between two subsequent pairs of pump and probe micropulses. When the liquid has moved by one spot size (400 μm, which approximately takes a time τ_{jet}), we expect the acoustic grating to be averaged or washed out. This is highlighted by the estimated residue in Fig. 3g, where we summed up $\frac{400\ \mu\mathrm{m}}{0.44\ \mu\mathrm{m}} \sim 909$ patterns like the single one shown in Fig. 2g, each shifted by the spatial offset of 0.44 μm. The resulting interference fringes at spatial and temporal overlap are shown in Fig. 3g. Please note that the amplitude of the pattern in Fig. 3g amounts to only 3% of the one shown in Fig. 2g. Thus, we expect that the signal from an acoustic grating at pump–probe overlap should only be present at the beginning of the pump macropulse, at $\tau \sim \tau_{\mathrm{ON}}$, when measuring the free-flowing jet. After the water has travelled one spot size, the remaining pump–probe signal cannot be attributed anymore to a diffraction grating, but rather to a nonlinear optical signal as indicated in Fig. 3f.

By taking into account a combination of acoustic and nonlinear effects, it is possible to account for the trend and the magnitude of the detected signal at pump–probe overlap in the water jet, see Fig. 3. The model, red curve in Fig. 3e, includes the same thermal component calculated previously without fitting parameters (the black curve in Fig. 3e) and includes an acoustic term $b\beta^2(^{\circ}T)(1 - s(\tau))$, where $b = -1.5 \times 10^4$ has the same value used for the water in the static cell (Fig. 2). We introduce the sigmoid function $s(\tau)$ to qualitatively account for the fact that the acoustic effects are present only close to $\tau \sim \tau_{\mathrm{ON}}$ and absent after the acoustic grating is washed out (Fig. 3g). The sigmoid function is $s(\tau) = \left(1 + \mathrm{e}^{\left(-\frac{\tau - \tau_{\mathrm{ON}} - c\cdot\tau_{\mathrm{jet}}}{d\cdot\tau_{\mathrm{jet}}}\right)}\right)^{-1}$, with c being a fitting parameter describing the middle point of the sigmoid (time at which the value of $s(\tau)$ is half of the maximum value), and d fitting parameter for the exponential slope, describing how steep $s(\tau)$ switches from maximum (1) to minimum (0). The results of the simulation obtained from the fitting parameters $c = 2$ and $d = 0.5$ are shown by the red curve in Fig. 3e and by the blue curve in Fig. 3f. After the acoustic grating vanishes at $\tau \sim 400$ μs, the pump–probe signal from the water jet becomes positive. We propose that this is the nonlinear optical signal, as shown in Fig. 3e and f. In our model, this signal is described by a transmission change defined by a quantity $a \cdot s(\tau)$, where $s(\tau)$ is the function described above and $a = \Delta T_{\mathrm{V}}/T_{\mathrm{V}} = +7\%$ is the magnitude of the nonlinear optical signal measured experimentally between about τ_{ON} + 100 μs ~ 470 μs and τ_{OFF}, see Fig. 3c. Overall, we find that a combination of acoustic and nonlinear optical signals is sufficient to account for the magnitude and the temporal evolution of the measured response by the liquid water jet, as can be seen by comparing the red curves in Fig. 3b and e, and the blue curves in Fig. 3c and f.

MD simulations suggest that optical phonon-like modes at THz frequencies can couple water[89] to proteins in solution.[23,90,91] Elton and Fernández-Serra[89] indicated that optical modes in the librational band of pure bulk water can propagate up to a distance of 2 nm. Conti-Nibali *et al.*[23,90] suggested that optical THz modes of a solvated protein spread to the hydration water, indicating an efficient solute–solvent coupling at these THz frequencies. The coupled protein–water acoustic modes were also investigated in more detail by Heyden *et al.*[91] These modes reveal correlated protein–water vibrations that extend up to 1 nm from the protein surface, which also depend on the specific chemistry of the protein surface. We note that the acoustic mode that has been emphasized in this work, and that is only relevant when the static cell is used, is not in the THz range but at the much lower frequency of 8.3 MHz. In fact, the frequency of the acoustic mode associated to the grating can be estimated by the speed of sound divided by the period of the interference pattern, *i.e.*, $\frac{1500\ \mathrm{m\ s^{-1}}}{180\ \mu\mathrm{m}} \sim 8.3$ MHz.

Previously,[27] we performed a full set of polarization-dependent experiments, and we estimated a lower limit for the third-order birefringence of bulk water, $\chi_e^{\,3} \sim 1.3 \times 10^{-15}\ \mathrm{cm^2\ V^{-2}}$, which is at least three orders of magnitude larger than the refractive response at VIS and NIR frequencies, see the first two rows of Table 1. This birefringent signal was estimated from[27] a transmission change of $\frac{\Delta T}{T} \sim 1\%$ (compare, *e.g.*, the dark and light blue curves in Fig. 2b of ref. 27) for $I_{\mathrm{Pu}} = 900\ \mathrm{MW\ cm^{-2}}$. Please

Table 1 Third-order response of bulk water (χ^3) *versus* frequency. Different techniques have been used: self-phase modulation (SPM), z-scan, self-focusing (SF), Kerr, third-harmonic generation (THG), pump–probe (Pp), polarization resolved pump–probe (pol-Pp). In the technique column we indicated whether the liquid sample used is enclosed in a static cell (static) or is flowing freely (jet). The response originating from the refraction change along one direction is ${\chi_n}^3$, from the difference between the refraction along two perpendicular directions is the birefringence, ${\chi_\varepsilon}^3$. The effective response, ${\chi_{\text{eff}}}^3$, is estimated from eqn (5) and the following parameters: $I_{\text{Pu}} \sim 50$ MW cm^{-2}, $\Delta T/T \sim 1.7\%$, $n_{\text{wat}} \sim 2$ for ref. 33; $I_{\text{Pu}} \sim 61$ MW cm^{-2}, $\Delta T/T \sim 2\%$, $n_{\text{wat}} \sim 2$ for ref. 28; and $I_{\text{Pu}} \sim 590$ MW cm^{-2} (estimated as[54] $I_{\text{Pu}} = E_{\text{THz}}^2/(2Z_0)$ with Z_0 vacuum impedance and peak field $E_{\text{THz}} = 0.5$ MV cm^{-1}), $\Delta T/T \sim 10\%$ (rough estimate from the ~10% drop in all optical constants reported at[35] 7 ps pump–probe delay for 0.5 MV cm^{-1}), $n_{\text{wat}} \sim 2$ for ref. 35

Frequency	Technique	χ^3 [cm^2 V^{-2}]	Ref.
Transient refraction along one axis, ${\chi_n}^3$			
VIS, NIR	SPM, z-scan, SF, Kerr, THG	${\chi_n}^3 \approx 2.6 \times 10^{-18}$	36–53
Transient birefringence, ${\chi_\varepsilon}^3$			
12.3 THz	pol-Pp, static	${\chi_\varepsilon}^3 \approx 1.3 \times 10^{-15}$	27
Effective total third-order response, ${\chi_{\text{eff}}}^3$			
12.3 THz	pol-Pp, jet	${\chi_{\text{eff}}}^3 \approx 7.2 \times 10^{-13}$	This work
1 THz	z-Scan, jet	${\chi_{\text{eff}}}^3 \approx 4.5 \times 10^{-13}$	32 and 33
1 THz	z-Scan, static	${\chi_{\text{eff}}}^3 \approx 4.4 \times 10^{-13}$	28
1 THz	Pp, jet	${\chi_{\text{eff}}}^3 \approx 2.3 \times 10^{-13}$	35

note that the single pump micropulse intensity used in ref. 27 is 9× times larger than the one used here. Given the fact that the nonlinear signals are proportional to the pump intensity,[27] we expect a birefringent signal of *ca.* 1%/9–0.11% for the experiments reported in the present study, which is below the noise level of ±0.5%. Thus, here we are unable to detect the birefringent component of the nonlinear signal. However, even given the lower pump intensity, the water jet reveals a large nonlinear signal, $\frac{\Delta T}{T} \sim +7\%$ (Fig. 3c).

Different experimental techniques are sensitive to different contributions to the total third-order response of a material. For example, some works[36–53] report the third-order response that depends only on the refraction change along one direction (${\chi_n}^3$), others the difference between the transient refraction along two perpendicular directions,[27] or birefringence, ${\chi_\varepsilon}^3$. In general, the third-order nonlinear THz signal of bulk water stems from the transient changes of both refraction as well as absorption.[28] In our case, the nonlinear signal is given by the difference between the red and black curves in Fig. 3b, as shown in blue in Fig. 3c. In order to compare it with previous results obtained with different experimental techniques, we introduce an effective total third-order coefficient, ${\chi_{\text{eff}}}^3$. A pump–probe signal originates from two pump photons with the same wavevector creating a population state.[61,92,93] The probe interacts with this population state and a nonlinear signal is generated in the probe direction. When a power detector is used, the probe heterodynes the nonlinear signal, and the intensity-dependent nonlinear transmission is $T^* \propto \left|E_{\text{sig}} + E_{\text{pr}}\right|^2 = \left|E_{\text{sig}}\right|^2 + \left|E_{\text{pr}}\right|^2 + 2\text{Re}\left[E_{\text{sig}}E_{\text{pr}}^*\right]$, where E_{pr} and E_{sig} are the electric fields of probe and nonlinear signal, respectively. Recalling that the signal is obtained by third-order mixing[61,92,93] ($E_{\text{sig}} \sim {\chi_{\text{eff}}}^3 E_{\text{Pu}} E_{\text{Pu}}^* E_{\text{pr}}$ with E_{Pu} pump field), that the probe intensity transmitted by the sample at equilibrium is $T \propto |E_{\text{pr}}|^2$, and assuming $E_{\text{sig}} \ll E_{\text{pr}}$, the relative variation of the transmission in a pump–probe experiment is $\frac{\Delta T}{T} = \frac{T^* - T}{T} \sim 2{\chi_{\text{eff}}}^3 |E_{\text{Pu}}|^2$. To the first approximation, if we use the relation between field amplitude and intensity of a monochromatic wave, $I = \frac{1}{2} cn\varepsilon_0 |E|^2$ with c speed of light, n index of refraction, and ε_0 vacuum permittivity, we obtain

$$\frac{\Delta T}{T} \approx \frac{4}{c \cdot n \cdot \varepsilon_0} \cdot {\chi_{\text{eff}}}^3 \cdot I_{\text{Pu}} \quad (5)$$

For the water jet we measured $\frac{\Delta T}{T} \sim +7\%$ (Fig. 3c), and by using eqn (5) with $I_{\text{Pu}} = 100$ MW cm^{-2} and[10] $n = n_{\text{wat}} = 1.55$, we estimate ${\chi_{\text{eff}}}^3 \sim 7.2 \times 10^{-13}$ cm^2 V^{-2} at 12.3 THz. This value is the largest reported to date for liquid water in the THz range and, as outlined in Table 1, is roughly twice as large as the ones reported by Tcypkin *et al.*[32,33] and Ghalgaoui *et al.*[35] at ~1 THz.

The cascaded intramolecular anharmonicity model proposed by Tcypkin *et al.*[32,33] neglected the librational contribution and displays a weak frequency dependence (see, *e.g.*, Fig. S7 in ref. 3). Thus, this model seems unable to explain the larger third-order response we found in liquid water at 12.3 THz. Let us now consider the field-ionization scenario proposed by Ghalgaoui *et al.*[35] Since the ponderomotive energy is inversely proportional to the frequency of the pump field,[35] the effect should be much smaller at 10 THz than at 1 THz. In fact, the ponderomotive energy of an electron driven by an external field with a field amplitude of 0.27 MV cm^{-1} at 12.3 THz should be more than 1000*x* smaller than in ref. 35, *i.e.*, we can exclude field-induced water ionization here. Conversely, the transient anisotropy model as introduced previously by us[27] predicts a smaller nonlinear response at 1 THz w.r.t. 12.3 THz and is, thus, qualitatively in agreement with all of the experimental observations reported to date.[27,28,32,33,35] The transient anisotropy should be larger at 12.3 THz, which is closer to the time scale of the reorientation relaxation as observed experimentally.

Conclusions

Previously, we reported[27] a giant transient birefringence in liquid water at 12.3 THz in a liquid cell. Here we report a comparison between the result in a cell and a liquid jet using longer macropulses, which allowed us to measure over longer time scales. While we were able to reproduce our previous observations (Fig. 1), we also investigated the different contributions to the transient change in the THz pump–probe response. Upon comparison of the results obtained on a static water cell (Fig. 2) with a free-flowing jet (Fig. 3) we suggest that the increase of the signal during the macropulse could originate from an acoustic phonon at 8.3 MHz. The anisotropic nonlinear signal observed here in the water jet at 12.3 THz confirms that driving the reorientation of hydrogen-bonded molecules induces a giant response, and it could help rationalize all the available nonlinear

experiments performed on water at THz frequencies.[27,28,32,33,35] As the rotationally damped motion of HB molecules in the librational band is resonantly driven at 12.3 THz, our results might open the door to the manipulation of solvation dynamics *via* strong fields, possibly also at interfaces. Considering that the technique outlined here is sensitive to ion hydration,[27] we suggest that it might also help to elucidate the dynamical properties of the hydration water of different anions and cations in future investigations.[94]

Author contributions

Conceptualization: F. N., M. H. Data curation: F. N., C. H., J. M. K. Formal analysis: F. N., C. H., J. M. K. Funding acquisition: M. H. Investigation: F. N., C. H., E. A., J. M. K. Methodology: F. N. Project administration: F. N. Resources: M. H., J. M. K. Software: F. N., C. H. Supervision: F. N., M. H. Validation: F. N., C. H., E. A. Visualization: F. N. Writing – original draft: F. N. Writing – review & editing: all authors.

Conflicts of interest

There are no conflicts to declare.

Acknowledgements

We acknowledge D. Welzel for experimental support. M. H. acknowledges funding by the ERC Advanced Grant 695437 "THz calorimetry". This work is part of the Cluster RESOLV funded by the Deutsche Forschungsgemeinschaft (DFG, German Research Foundation) under Germany's Excellence Strategy–EXC 2033–390677874–RESOLV.

Notes and references

1 P. Ball, Water—an enduring mystery, *Nature*, 2008, **452**, 291–292.
2 P. Gallo, K. Amann-Winkel, C. A. Angell, M. A. Anisimov, F. Caupin, C. Chakravarty, E. Lascaris, T. Loerting, A. Z. Panagiotopoulos, J. Russo, J. A. Sellberg, H. E. Stanley, H. Tanaka, C. Vega, L. Xu and L. G. M. Pettersson, Water: A Tale of Two Liquids, *Chem. Rev.*, 2016, **116**, 7463–7500.
3 A. Nilsson and L. G. M. Pettersson, The structural origin of anomalous properties of liquid water, *Nat. Commun.*, 2015, **6**, 8998.
4 C. A. Angell, Insights into Phases of Liquid Water from Study of Its Unusual Glass-Forming Properties, *Science*, 2008, **319**, 582–587.
5 M. Cho, G. R. Fleming, S. Saito, I. Ohmine and R. M. Stratt, Instantaneous normal mode analysis of liquid water, *J. Chem. Phys.*, 1994, **100**, 6672–6683.
6 M. Heyden, J. Sun, S. Funkner, G. Mathias, H. Forbert, M. Havenith and D. Marx, Dissecting the THz spectrum of liquid water from first principles via correlations in time and space, *Proc. Natl. Acad. Sci. U. S. A.*, 2010, **107**, 12068–12073.
7 F. Novelli, B. Guchhait and M. Havenith, Towards Intense THz Spectroscopy on Water: Characterization of Optical Rectification by GaP, OH1, and DSTMS at OPA Wavelengths, *Materials*, 2020, **13**, 1311.
8 D. J. Cook, J. X. Chen, E. A. Morlino and R. M. Hochstrasser, Terahertz-field-induced second-harmonic generation measurements of liquid dynamics, *Chem. Phys. Lett.*, 1999, **309**, 221–228.
9 H. Elgabarty and T. D. Kühne, Tumbling with a limp: local asymmetry in water's hydrogen bond network and its consequences, *Phys. Chem. Chem. Phys.*, 2020, **22**, 10397–10411.
10 H. R. Zelsmann, Temperature dependence of the optical constants for liquid H2O and D2O in the far IR region, *J. Mol. Struct.*, 1995, **350**, 95–114.
11 W. J. Ellison, Permittivity of Pure Water, at Standard Atmospheric Pressure, over the Frequency Range 0–25THz and the Temperature Range 0–100 °C, *J. Phys. Chem. Ref. Data*, 2007, **36**, 1–18.
12 I. Bergonzi, L. Mercury, J.-B. Brubach and P. Roy, Gibbs free energy of liquid water derived from infrared measurements, *Phys. Chem. Chem. Phys.*, 2014, **16**, 24830–24840.
13 J. E. Bertie and Z. Lan, Infrared Intensities of Liquids XX: The Intensity of the OH Stretching Band of Liquid Water Revisited, and the Best Current Values of the Optical Constants of H_2O(l) at 25 °C between 15 000 and 1 cm^{-1}, *Appl. Spectrosc.*, 1996, **50**, 1047–1057.
14 J.-J. Max and C. Chapados, Isotope effects in liquid water by infrared spectroscopy. III. H_2O and D_2O spectra from 6000 to 0 cm^{-1}, *J. Chem. Phys.*, 2009, **131**, 184505.
15 P. Lunkenheimer, S. Emmert, R. Gulich, M. Köhler, M. Wolf, M. Schwab and A. Loidl, Electromagnetic-radiation absorption by water, *Phys. Rev. E*, 2017, **96**, 062607.
16 D. R. Martin and D. V. Matyushov, Terahertz absorption of lysozyme in solution, *J. Chem. Phys.*, 2017, **147**, 084502.
17 S. Ebbinghaus, S. J. Kim, M. Heyden, X. Yu, U. Heugen, M. Gruebele, D. M. Leitner and M. Havenith, An extended dynamical hydration shell around proteins, *Proc. Natl. Acad. Sci. U. S. A.*, 2007, **104**, 20749–20752.
18 Y. He, P. I. Ku, J. R. Knab, J. Y. Chen and A. G. Markelz, Protein dynamical transition does not require protein structure, *Phys. Rev. Lett.*, 2008, **101**, 2–5.
19 G. Acbas, K. A. Niessen, E. H. Snell and A. G. Markelz, Optical measurements of long-range protein vibrations, *Nat. Commun.*, 2014, **5**, 3076.
20 K. A. Niessen, M. Xu, D. K. George, M. C. Chen, A. R. Ferré-D'Amaré, E. H. Snell, V. Cody, J. Pace, M. Schmidt and A. G. Markelz, Protein and RNA dynamical fingerprinting, *Nat. Commun.*, 2019, **10**, 1–10.
21 J. W. Bye, S. Meliga, D. Ferachou, G. Cinque, J. A. Zeitler and R. J. Falconer, Analysis of the Hydration Water around Bovine Serum Albumin Using Terahertz Coherent Synchrotron Radiation, *J. Phys. Chem. A*, 2014, **118**, 83–88.
22 J. Monroe, M. Barry, A. DeStefano, P. A. Gokturk, S. Jiao, D. Robinson-Brown, T. Webber, E. J. Crumlin, S. Han,

M. S. Shell, P. Aydogan Gokturk, S. Jiao, D. Robinson-Brown, T. Webber, E. J. Crumlin, S. Han and M. S. Shell, Water Structure and Properties at Hydrophilic and Hydrophobic Surfaces, *Annu. Rev. Chem. Biomol. Eng.*, 2020, **11**, 1–35.

23 V. Conti Nibali and M. Havenith, New Insights into the Role of Water in Biological Function: Studying Solvated Biomolecules Using Terahertz Absorption Spectroscopy in Conjunction with Molecular Dynamics Simulations, *J. Am. Chem. Soc.*, 2014, **136**, 12800–12807.

24 K. J. Tielrooij, N. Garcia-Araez, M. Bonn and H. J. Bakker, Cooperativity in Ion Hydration, *Science*, 2010, **328**, 1006–1009.

25 P. Zalden, L. Song, X. Wu, H. Huang, F. Ahr, O. D. Mücke, J. Reichert, M. Thorwart, P. K. Mishra, R. Welsch, R. Santra, F. X. Kärtner and C. Bressler, Molecular polarizability anisotropy of liquid water revealed by terahertz-induced transient orientation, *Nat. Commun.*, 2018, **9**, 2142.

26 H. Elgabarty, T. Kampfrath, D. J. Bonthuis, V. Balos, N. K. Kaliannan, P. Loche, R. R. Netz, M. Wolf, T. D. Kühne and M. Sajadi, Energy transfer within the hydrogen bonding network of water following resonant terahertz excitation, *Sci. Adv.*, 2020, **6**, eaay7074.

27 F. Novelli, L. Ruiz Pestana, K. C. Bennett, F. Sebastiani, E. M. Adams, N. Stavrias, T. Ockelmann, A. Colchero, C. Hoberg, G. Schwaab, T. Head-Gordon and M. Havenith, Strong Anisotropy in Liquid Water upon Librational Excitation Using Terahertz Laser Fields, *J. Phys. Chem. B*, 2020, **124**, 4989–5001.

28 F. Novelli, C. Y. Ma, N. Adhlakha, E. M. Adams, T. Ockelmann, D. Das Mahanta, P. Di Pietro, A. Perucchi and M. Havenith, Nonlinear terahertz transmission by liquid water at 1 THz, *Appl. Sci.*, 2020, **10**, 20–23.

29 H. Zhao, Y. Tan, R. Zhang, Y. Zhao, C. Zhang and L. Zhang, Anion–water hydrogen bond vibration revealed by the terahertz Kerr effect, *Opt. Lett.*, 2021, **46**, 230.

30 H. Zhao, Y. Tan, L. Zhang, R. Zhang, M. Shalaby, C. Zhang, Y. Zhao and X.-C. Zhang, Ultrafast hydrogen bond dynamics of liquid water revealed by terahertz-induced transient birefringence, *Light: Sci. Appl.*, 2020, **9**, 136.

31 M. Zhukova, M. Melnik, I. Vorontsova, A. Tcypkin and S. Kozlov, Estimations of low-inertia cubic nonlinearity featured by electro-optical crystals in the thz range, *Photonics*, 2020, **7**, 1–7.

32 A. Tcypkin, M. Zhukova, M. Melnik, I. Vorontsova, M. Kulya, S. Putilin, S. Kozlov, S. Choudhary and R. W. Boyd, Giant Third-Order Nonlinear Response of Liquids at Terahertz Frequencies, *Phys. Rev. Appl.*, 2021, **15**, 054009.

33 A. N. Tcypkin, M. V. Melnik, M. O. Zhukova, I. O. Vorontsova, S. E. Putilin, S. A. Kozlov and X.-C. Zhang, High Kerr nonlinearity of water in THz spectral range, *Opt. Express*, 2019, **27**, 10419.

34 S. Ashihara, N. Huse, A. Espagne, E. T. J. J. Nibbering and T. Elsaesser, Ultrafast Structural Dynamics of Water Induced by Dissipation of Vibrational Energy, *J. Phys. Chem. A*, 2007, **111**, 743–746.

35 A. Ghalgaoui, L.-M. Koll, B. Schütte, B. P. Fingerhut, K. Reimann, M. Woerner and T. Elsaesser, Field-Induced Tunneling Ionization and Terahertz-Driven Electron Dynamics in Liquid Water, *J. Phys. Chem. Lett.*, 2020, **11**, 7717–7722.

36 Z. W. Wilkes, S. Varma, Y. H. Chen, H. M. Milchberg, T. G. Jones and A. Ting, Direct measurements of the nonlinear index of refraction of water at 815 and 407 nm using single-shot supercontinuum spectral interferometry, *Appl. Phys. Lett.*, 2009, **94**, 1–4.

37 B. A. Rockwell, W. P. Roach, M. E. Rogers and M. W. Mayo, C. a Toth, C. P. Cain and G. D. Noojin, Nonlinear refraction in vitreous humor, *Opt. Lett.*, 1993, **18**, 1792–1794.

38 N. J. Harrison and B. R. Jennings, Laser-induced birefringence measurement for pure liquids, *Meas. Sci. Technol.*, 1992, **3**, 120–125.

39 P. P. Ho and R. R. Alfano, Optical Kerr effect in liquids, *Phys. Rev. A: At., Mol., Opt. Phys.*, 1979, **20**, 2170–2187.

40 F. Kajzar and J. Messier, Third-harmonic generation in liquids, *Phys. Rev. A: At., Mol., Opt. Phys.*, 1985, **32**, 2352–2363.

41 D. Débarre and E. Beaurepaire, Quantitative characterization of biological liquids for third-harmonic generation microscopy, *Biophys. J.*, 2007, **92**, 603–612.

42 V. Shcheslavskiy, G. Petrov and V. V. Yakovlev, Nonlinear optical susceptibility measurements of solutions using third-harmonic generation on the interface, *Appl. Phys. Lett.*, 2003, **82**, 3982–3984.

43 R. Barille, L. Canioni, L. Sarger and G. Rivoire, Nonlinearity measurements of thin films by third-harmonic-generation microscopy, *Phys. Rev. E: Stat., Nonlinear, Soft Matter Phys.*, 2002, **66**, 067602.

44 B. M. Novac, F. A. Banakhr, I. R. Smith, L. Pécastaing, R. Ruscassié, A. S. De Ferron and P. Pignolet, Determination of the Kerr Constant of Water at 658 nm for Pulsed Intense Electric Fields, *IEEE Trans. Plasma Sci.*, 2012, **40**, 2480–2490.

45 R. K. Khanna, E. Dempsey and G. Parry, Jones, Kerr constant of water from 280 to 350 K at 632.8 nm, *Chem. Phys. Lett.*, 1978, **53**, 542–544.

46 W. L. Smith, P. Liu and N. Bloembergen, Superbroadening in H_2O and D_2O by self focused picosecond pulses from a YAIG: ND laser, *Phys. Rev. A: At., Mol., Opt. Phys.*, 1977, **15**, 2396–2403.

47 Z. Blaszczak and P. Gauden, Method for the determination of the value of the optical Kerr constant in weakly anisotropic liquids, *Rev. Sci. Instrum.*, 1987, **58**, 1949–1951.

48 N. J. Harrison and B. R. Jennings, Laser-Induced Kerr Constants for Pure Liquids, *J. Phys. Chem. Ref. Data*, 1992, **21**, 157–163.

49 T. Y. F. Tsang, Optical third-harmonic generation at interfaces, *Phys. Rev. A: At., Mol., Opt. Phys.*, 1995, **52**, 4116–4125.

50 O. Clay, C. B. Schaffer, J. A. Squier and D. Kleinfeld, in *SPIE Commercial and Biomedical Applications of Ultrafast Lasers VI*, ed. J. Neev, S. Nolte, A. Heisterkamp and C. B. Schaffer, 2006, vol. 6008, p. 610809.

51 A. Brodeur and S. L. Chin, Band-Gap Dependence of the Ultrafast White-Light Continuum, *Phys. Rev. Lett.*, 1998, **80**, 4406–4409.

52 E. T. J. Nibbering, M. A. Franco, B. S. Prade, G. Grillon, C. Le Blanc and A. Mysyrowicz, Measurement of the nonlinear

refractive index of transparent materials by spectral analysis after nonlinear propagation, *Opt. Commun.*, 1995, **119**, 479–484.
53 W. Liu, O. Kosareva, I. S. Golubtsov, A. Iwasaki, A. Becker, V. P. Kandidov and S. L. Chin, Femtosecond laser pulse filamentation versus optical breakdown in H_2O, *Appl. Phys. B: Lasers Opt.*, 2003, **76**, 215–229.
54 B. Liu, H. Bromberger, A. Cartella, T. Gebert, M. Först and A. Cavalleri, Generation of narrowband, high-intensity, carrier-envelope phase-stable pulses tunable between 4 and 18 THz, *Opt. Lett.*, 2017, **42**, 129.
55 P. Keblinski, D. G. Cahill, A. Bodapati, C. R. Sullivan and T. A. Taton, Limits of localized heating by electromagnetically excited nanoparticles, *J. Appl. Phys.*, 2006, **100**, 1–6.
56 H. H. Richardson, M. T. Carlson, P. J. Tandler, P. Hernandez and A. O. Govorov, Experimental and theoretical studies of light-to-heat conversion and collective heating effects in metal nanoparticle solutions, *Nano Lett.*, 2009, **9**, 1139–1146.
57 Z. Qin and J. C. Bischof, Thermophysical and biological responses of gold nanoparticle laser heating, *Chem. Soc. Rev.*, 2012, **41**, 1191–1217.
58 T. Q. Luong, Y. Xu, E. Bründermann, D. M. Leitner and M. Havenith, Hydrophobic collapse induces changes in the collective protein and hydration low frequency modes, *Chem. Phys. Lett.*, 2016, **651**, 1–7.
59 M. Tsubouchi, H. Hoshina, M. Nagai and G. Isoyama, Plane photoacoustic wave generation in liquid water using irradiation of terahertz pulses, *Sci. Rep.*, 2020, **10**, 18537.
60 S. Yamazaki, M. Harata, Y. Ueno, M. Tsubouchi, K. Konagaya, Y. Ogawa, G. Isoyama, C. Otani and H. Hoshina, Propagation of THz irradiation energy through aqueous layers: Demolition of actin filaments in living cells, *Sci. Rep.*, 2020, **10**, 9008.
61 R. W. Boyd, *Nonlinear Optics*, Academic Press, 3rd edn, 2007.
62 D. I. Kovsh, D. J. Hagan and E. W. Van, Stryland, Numerical modeling of thermal refraction in liquids in the transient regime, *Opt. Express*, 1999, **4**, 315.
63 A. Vogel and V. Venugopalan, Mechanisms of pulsed laser ablation of biological tissues, *Chem. Rev.*, 2003, **103**, 577–644.
64 C. Tian, Z. Xie, M. L. Fabiilli, S. Liu, C. Wang, Q. Cheng and X. Wang, Dual-pulse nonlinear photoacoustic technique: a practical investigation, *Biomed. Opt. Express*, 2015, **6**, 2923.
65 A. D. Kraus and A. Bejan, *Heat Transfer Handbook*, John Wiley & Sons, Inc., Hoboken, New Jersey, 2003.
66 G. Paltauf and H. Schmidt-Kloiber, Microcavity dynamics during laser-induced spallation of liquids and gels, *Appl. Phys. A: Mater. Sci. Process.*, 1996, **62**, 303–311.
67 R. J. D. Miller, R. Casalegno, K. A. Nelson and M. D. Fayer, Laser-induced ultrasonics: A dynamic holographic approach to the measurement of weak absorptions, optoelastic constants and acoustic attenuation, *Chem. Phys.*, 1982, **72**, 371–379.
68 E. Hecht, *Optics*, Pearson, 5th edn, 2017.
69 Appendix B Thermophysical Properties of Water, in *Drying Phenomena*, John Wiley & Sons, Ltd, 2015, pp. 457–459, DOI: 10.1002/9781118534892.app2.
70 F. Sedlmeier, S. Shadkhoo, R. Bruinsma and R. R. Netz, Charge/mass dynamic structure factors of water and applications to dielectric friction and electroacoustic conversion, *J. Chem. Phys.*, 2014, **140**, 054512.
71 V. E. Gusev and A. A. Karabutov, *Laser Optoacoustics*, American Institute of Physics, New York, 1991.
72 S. Å. Ellingsen and I. Brevik, Electrostrictive fluid pressure from a laser beam, *Phys. Fluids*, 2011, **23**, 096101.
73 I. Brevik, Experiments in phenomenological electrodynamics and the electromagnetic energy-momentum tensor, *Phys. Rep.*, 1979, **52**, 133–201.
74 I. Brevik, Radiation forces and the Abraham-Minkowski problem, *Mod. Phys. Lett. A*, 2018, **33**, 1–15.
75 A. B. Gojani, R. Bejtullahu and S. Obayashi, On two optomechanical effects of laser-induced electrostriction in dielectric liquids, *Jpn. J. Appl. Phys.*, 2014, **53**, 092703.
76 J. Prakash, M. M. Seyedebrahimi, A. Ghazaryan, J. Malekzadeh-Najafabadi, V. Gujrati and V. Ntziachristos, Short-wavelength optoacoustic spectroscopy based on water muting, *Proc. Natl. Acad. Sci. U. S. A.*, 2020, **117**, 4007–4014.
77 A. Vogel, N. Linz, S. Freidank and G. Paltauf, Femtosecond-laser-induced nanocavitation in water: Implications for optical breakdown threshold and cell surgery, *Phys. Rev. Lett.*, 2008, **100**, 1–4.
78 H. Eichler and H. Stahl, Time and frequency behavior of sound waves thermally induced by modulated laser pulses, *J. Appl. Phys.*, 1973, **44**, 3429–3435.
79 K. A. Nelson, R. J. D. D. Miller, D. R. Lutz and M. D. Fayer, Optical generation of tunable ultrasonic waves, *J. Appl. Phys.*, 1982, **53**, 1144–1149.
80 Q. Shen, A. Harata and T. Sawada, Theory of Transient Reflecting Grating in Fluid/Metallic Thin Film/Substrate Systems for Thin Film Characterization and Electrochemical Investigation, *Jpn. J. Appl. Phys.*, 1996, **35**, 2339–2349.
81 K. A. Nelson and M. D. Fayer, Laser induced phonons: A probe of intermolecular interactions in molecular solids, *J. Chem. Phys.*, 1980, **72**, 5202–5218.
82 K. A. Nelson, R. Casalegno, R. J. D. Miller and M. D. Fayer, Laser-induced excited state and ultrasonic wave gratings: Amplitude and phase grating contributions to diffraction, *J. Chem. Phys.*, 1982, **77**, 1144–1152.
83 D. Kim, M. Ye and C. P. Grigoropoulos, Pulsed laser-induced ablation of absorbing liquids and acoustic-transient generation, *Appl. Phys. A: Mater. Sci. Process.*, 1998, **67**, 169–181.
84 S. C. Santucci, D. Fioretto, L. Comez, A. Gessini and C. Masciovecchio, Is there any fast sound in water?, *Phys. Rev. Lett.*, 2006, **97**, 1–4.
85 H. J. Eichler, P. Günter and D. W. Pohl, *Laser-Induced Dynamic Gratings*, Springer-Verlag, Berlin Heidelberg GmbH, 1986.
86 N. Gedik, J. Orenstein, R. Liang, D. A. Bonn and W. N. Hardy, Diffusion of Nonequilibrium Quasi-Particles in a Cuprate Superconductor, *Science*, 2003, **300**, 1410–1412.
87 N. Gedik, J. Orenstein, R. Liang, D. A. Bonn and W. N. Hardy, Transient Gratings Formed by Nonequilibrium Quasiparticles in $YBa_2Cu_3O_{6.5}$, *J. Supercond.*, 2004, **17**, 117–120.

88 C. A. Dennett and M. P. Short, Thermal diffusivity determination using heterodyne phase insensitive transient grating spectroscopy, *J. Appl. Phys.*, 2018, **123**, 215109.
89 D. C. Elton and M. Fernández-Serra, The hydrogen-bond network of water supports propagating optical phonon-like modes, *Nat. Commun.*, 2016, **7**, 10193.
90 V. Conti Nibali, G. D'Angelo, A. Paciaroni, D. J. Tobias and M. Tarek, On the Coupling between the Collective Dynamics of Proteins and Their Hydration Water, *J. Phys. Chem. Lett.*, 2014, **5**, 1181–1186.
91 M. Heyden and D. J. Tobias, Spatial Dependence of Protein-Water Collective Hydrogen-Bond Dynamics, *Phys. Rev. Lett.*, 2013, **111**, 218101.
92 P. Hamm, Principles of Nonlinear Optical Spectroscopy: A Practical Approach or: Mukamel for Dummies, 2005.
93 S. Mukamel, *Principles of Nonlinear Optical Spectroscopy*, Oxford University Press, New York, 1995.
94 G. Schwaab, F. Sebastiani, M. Havenith, M. Havenith-Newen, G. Schwaab and F. Sebastiani, Ion Hydration and Ion Pairing as Probed by THz Spectroscopy, *Angew. Chem., Int. Ed.*, 2019, **58**, 3000–3013.